Water Research 112 (2017) 236–247

Contents lists available at ScienceDirect

Water Research

journal homepage: www.elsevier.com/locate/watres

Activation of persulfates by natural magnetic pyrrhotite for water disinfection: Efficiency, mechanisms, and stability

Dehua Xia [a], Yan Li [b], Guocheng Huang [a], Ran Yin [c], Taicheng An [d, **], Guiying Li [d], Huijun Zhao [e, f], Anhuai Lu [g], Po Keung Wong [a, *]

[a] School of Life Sciences, The Chinese University of Hong Kong, Shatin, NT, Hong Kong, China
[b] The Key Laboratory of Orogenic Belts and Crustal Evolution, School of Earth and Space Sciences, Peking University, Beijing, 100871, China
[c] Department of Civil and Environmental Engineering, The Hong Kong University of Science and Technology, Clear Water Bay, Kowloon, Hong Kong SAR, China
[d] Institute of Environmental Health and Pollution Control, School of Environmental Science and Engineering, Guangdong University of Technology, Guangzhou, 510006, Guangdong, China
[e] Centre for Clean Environment and Energy, Griffith Scholl of Environment, Griffith University, Queensland, 4222, Australia
[f] Laboratory of Nanomaterials and Nanostructures, Institute of Solid State Physics, Chinese Academy of Sciences, Hefei, 230031, Anhui, China
[g] School of Geoscience and Info-Physics, Central South University, Changsha, 410083, China

ARTICLE INFO

Article history:
Received 25 November 2016
Received in revised form
21 January 2017
Accepted 25 January 2017
Available online 30 January 2017

Keywords:
Natural pyrrhotite
Persulfate
Sulfate radical
Water disinfection
Heterogeneous catalysis

ABSTRACT

This study introduces natural occurring magnetic pyrrhotite (NP) as an environmentally friendly, easy available, and cost-effective alternative catalyst to activate persulfate (PS) of controlling microbial water contaminants. The *E. coli* K-12 inactivation kinetics observed in batch experiments was well described with first-order reaction. The optimum inactivation rate ($k = 0.47$ log/min) attained at a NP dose of 1 g/L and a PS dose of 1 mM, corresponding to total inactivation of 7 $\log_{10}$ cfu/mL cells within 15 min. Measured k increased > 2-fold when temperature increased from 20 to 50 °C; and > 4-fold when pH decreased from 9 to 3. Aerobic conditions were more beneficial to cell inactivation than anaerobic conditions due to more reactive oxygen species (ROS) generated. ROS responsible for the inactivation were identified to be $^{\bullet}SO_4^-$ > $^{\bullet}OH$ > H_2O_2 based on a positive scavenging test and *in situ* ROS determination. *In situ* characterization suggested that PS effectively bind to NP surface was likely to form charge transfer complex ($\equiv Fe(II)\cdots O_3SO{-}OSO_3^-$), which mediated ROS generation and *E. coli* K-12 oxidation. The increased cell-envelope lesions consequently aggravated intracellular protein depletion and genome damage to cause definite bacterial death. The NP still maintained good physiochemical structure and stable activity even after 4 cycle. Moreover, NP/PS system also exhibited good *E. coli* K-12 inactivation efficiency in authentic water matrices like surface water and effluents of secondary wastewater.

1. Introduction

With increasing populations and uncertain global climate changes, the shortages of fresh and sanitary water require increased water recycle and reuse (Rietveld et al., 2011; Haaken et al., 2014). Biohazards such as bacteria, viruses, and fungi are widely presented in wastewater, which can cause a variety of water-borne diseases to humans and animals (Dobrowsky et al., 2014; Soller et al., 2014). Unfortunately, conventional water disinfection technologies, including chlorination, ozone, and ultraviolet (UV), have some disadvantages during application. For instance, a number of biohazards are naturally resistant to UV and chlorination (Eischeid et al., 2011; Rizzo et al., 2013a,b); the toxic and corrosive characteristics of ozone limit its practical application (Anastasi et al., 2013); the formation of disinfection byproducts (DBPs) by chlorination and ozonation are with potential carcinogenicity or toxicity (Parker et al., 2014; Sharma et al., 2014). Therefore, effectively removing biohazards from water is a challenge that has received great attention (Sun et al., 2014; Huang et al., 2017), and versatile new technologies are highly needed to simultaneously inactivate biohazards and eliminate disinfection debris.

* Corresponding author.
** Corresponding author.
E-mail addresses: antc99@gdut.edu.cn (T. An), pkwong@cuhk.edu.hk (P.K. Wong).

http://dx.doi.org/10.1016/j.watres.2017.01.052
0043-1354/

In recent decades, sulfate radicals ($\cdot SO_4^-$) based advanced oxidation process (AOP) has attracted increasing interests in water treatment, due to their high efficiency in degrading a wide range of recalcitrant micro-contaminants (Drzewicz et al., 2012; Yuan et al., 2014) and even inactivating biohazards (Anipsitakis et al., 2008; Tsitonaki et al., 2008; Chesney et al., 2016). For instance, Michael-Kordatou et al. (2015a) evidence that the UVC/PS process can result in rapid and complete erythromycin (ERY) degradation and ERY-resistant *Escherichia coli* inactivation in secondary treated wastewater, thus to produce a final treated effluent with lower phytotoxicity (<10%) compared to the untreated wastewater. The good performance of $\cdot SO_4^-$ based AOP in wastewater is mainly attributed to the large formation of highly reactive species, such as $\cdot SO_4^-$ (2.5–3.1 eV) and its derived •OH (2.7 eV) occurring in natural conditions (Michael-Kordatou et al., 2015a). Moreover, Ahn et al. (2013) use zero valent iron (ZVI) to activate persulfate (PS, $S_2O_8^{2-}$) for disinfecting ballast water and achieve a result that the marine phytoplankton could be totally inactivated and mineralized without formation of harmful byproducts. In analogy, $\cdot SO_4^-$ based AOP may hold promise to be more effective than conventional water disinfection processes in inactivating biohazards due to their more powerful oxidation capabilities and lower tendency to form DBPs.

Generally, $\cdot SO_4^-$ can be produced by the activation of PS and PMS (Wang et al., 2015; Zhong et al., 2015; Feng et al., 2016). Approaches of PS/PMS activation mainly include heat, microwave, UV, and addition of transition metals or carbon materials (Waldemer et al., 2007; Johnson et al., 2008; Guan et al., 2011; Matzek and Carter, 2016). Especially, the utilization of transition metal (zero valent iron, Co_3O_4, CuO/Fe_3O_4, etc.) has received particular attention to heterogeneously activate PS/PMS, because they are not consumed during the activation and no additional energy is required (Guan et al., 2013; Zhang et al., 2013; Zeng et al., 2015; Oh et al., 2016). However, many limitations for the wide-span application of these synthetic catalysts still exist: (1) the complex fabrication procedure and expensive massive production of these catalysts (Wang et al., 2014); (2) the potential leaching of heavy metals in the synthetic catalysts like Co^{2+} or Cu^{2+} are hazardous to environment (Hu et al., 2012; Ren et al., 2015); (3) the recycle and reuse of these nano-size catalyst is difficult. Therefore, developing new catalysts for further decreasing the cost of synthesis, potential secondary pollution, and easy recycle is necessary.

Naturally occurring minerals enriched in transition metals may provide an economical alternative for practical water treatment, as which can be readily supplied in large quantities at low cost (Teel et al., 2011; Yan et al., 2015). In this work, natural pyrrhotite (NP, $Fe_{1-x}S$) is suggested to be a good catalyst to effectively activate PS/PMS for water treatment: the great involvement of Fe^{2+} in NP is beneficial for PS activation and the leached Fe ions are environmental friendly, as well as the specific ferromagnetic properties can facilitate its separation and recycling after utilization (Xia et al., 2015a). In fact, NP is widely dispersed in natural settings and always discarded as a waste due to its over-supply in the sulfuric acid market (Yang et al., 2014). Therefore, it is beneficial to investigate the PS/PMS activation ability of reusing NP waste for both water treatment and mine tailing remediation. Moreover, there still exists contradictory interpretations with respect to the identity of the reactive species and the PS/PMS activation mechanisms (i.e., radical vs non-radical mechanisms, Zhang et al., 2014), which also need to be analyze when NP was involved for PS/PMS activation.

In this work, natural pyrrhotite was first utilized to activate PS for *E. coli* K-12 inactivation, a model bacterial strains in water (Xia et al., 2015b). To test the activity and applicability of NP/PS system, the inactivation kinetics of *E. coli* K-12 were measured at varying cell density, NP/PS dose, temperature, pH, bicarbonate, authentic wastewater matrix, etc. Meanwhile, its efficiency in terms of radical type and yield, as well as *in situ* ATR-FTIR characterization and chronoamperometric measurements, were collectively applied to analyze the PS activation process occurring on the NP surface. Moreover, microscope was applied to assess damage to cell envelope, and biomolecule assay was utilized to monitor the destruction of cytoplasmic proteins and chromosomal DNA during treatment. Furthermore, the reusability and structural stability of recycled NP were also analyzed. This work may provide a cost-effective method for biohazards inactivation in water-scarce regions, where the wastewater reuse schemes was implemented like agricultural irrigation (Michael-Kordatou et al., 2015a,b).

2. Materials and methods

2.1. Chemicals

Pristine natural pyrrhotite (NP) mineral was collected from a mining site in Inner Mongolia province, China. Chemical scavengers included methanol (Sigma-Aldrich, USA), tert-butanol alcohol (TBA, Sigma-Aldrich, USA), Fe(II)-EDTA (prepared with $FeSO_4$ and Na_2EDTA, Ajax Chemicals, Australia) and TEMPOL (Fuchen, China). Sodium persulfate (PS), 5,5-dimethyl-1-pyrrolidine *N*-oxide (DMPO) were purchased from Aladdin, China. All reagents used were at least analytical grade and prepared in ultrapure water (Millipore, Molsheim France).

2.2. Characterization

The X-ray powder diffraction (XRD) spectra of the NP was recorded on a Bruker D8 Advance X-ray powder diffractometer (Bruker Co., Ltd.). The surface morphology of NP was characterized with a Hitachi S-4800 field emission scanning electron microscope (SEM). The valence states of Fe in NP were examined with an ESCALAB 250XI X-ray photoelectron spectroscopy (XPS, Thermo). The magnetic properties of NP were determined by vibrating sample magnetometer (VSM-7300, Quantum design, Lakeshore, USA) at 25 °C. The *in situ* ATR-FTIR spectra of the NP was recorded on a Nicolet Fourier transform infrared spectrometer (Magna-IR 750) equipped with a Universal ATR accessory. Purified water was used to identify background noise. The spectra of the NP catalysts were calibrated by subtracting the spectrum of purified water during the scanning processes. Details are listed as follows: First, 50 mg of NP was mixed with 10 mL purified water or PS solution (0.5 mM). After a reaction time of 5 min, the solid particles from the suspensions were scanned in the wavenumber range of 800–4000 1/cm at a resolution of 4 1/cm. The leached metal ions were quantified by inductively coupled plasma-optical emission spectrometer (ICP-OES, ULTIMA 2000, HORIDA). The chemical compositions of several randomly selected mineral particles were characterized by electron microprobe analyses (EMPA, JEOL JCXA 733) at China University of Geosciences (Beijing).

2.3. Experimental procedure

Escherichia coli K-12 (Gram -ve, *E. coli* K-12) and *Staphylococcus aureus* (Gram + ve, *S. aureus*) were chosen as model bacterium to evaluate the inactivation ability of NP/PS system. The bacterial cells were cultured in nutrient broth (BioLife, Milano, Italy) at 37 °C with shaking, then harvested in the late exponential phase of growth. The harvested bacteria were centrifuged at 1000 rpm for 1 min, and the pellets were resuspended in ultrapure water and recentrifuged at 1000 rpm for 1 min to remove the growth medium, then the final pellets were resuspended in ultrapure water for experiment. A 50 mL suspension including NP of 50 mg and *E. coli* K-12 of

2×10^7 cfu (colony forming unit)/mL in a flask was vigorously dispersed by a magnetic stirrer, followed by adding PS (0–2 mM) to start the reaction. Aliquot samples were collected at different time intervals and diluted serially with sterilized saline solution, then immediately spread on the nutrient agar (Lab M, Lancashire, UK) plate. All the plates were incubated at 37 °C for 24 h. Control experiments with NP or PS alone were also conducted in triplicate, and the detection limit of spread plate was 1 cfu/mL. To analyze the influence of pH, appropriate amounts of H_2SO_4 (0.1 M) or NaOH (0.1 M) was added to adjust the initial pH. Bacterial inactivation was also conducted in authentic water matrix, including surface water and effluents of secondary wastewater, the detailed water parameters were shown in Table S1 (Supporting Information). Prior to use, the water samples were filtered by glass fiber filters.

2.4. Analyses

(i) Electron paramagnetic resonance (EPR) analysis: A solution containing 10 mM DMPO, 0.5 mM PS was prepared, and then 50 mg NP was added to initiate the reaction. After 0, 5, 10 min of reaction, samples were taken and analyzed on a JEOL FA200 EPR spectrometer; (ii) $^{\bullet}O_2^-$ was quantitatively analyzed by detecting the decrease in the concentration of nitro blue tetrazolium (NBT, $k = 5.88 \times 10^4$ M^{-1} s^{-1}) at a wavelength of 259 nm with a UV–vis spectrophotometer (LabTech); (iii) H_2O_2 was analyzed on a Hitachi F-4500 fluorescence spectrophotometer based on the reaction of H_2O_2 with courmarin to form a high fluorescent compound (7-hydroxylcoumarin, 456 nm); (iv) Cell viability assay: *E. coli* K-12 cells treated at various times were tested using a LIVE/DEAD®-BacLight Bacterial Viability Kit (Molecular Probes, USA) with a fluorescence microscope; (v) Determination of cellular ATP levels: *E. coli* K-12 cells treated at various times were assayed for adenosine triphosphate (ATP) by a luciferin/luciferase test (Bac-Titer-Glo Microbial Cell Viability Assay Kit, Promega), and the luminescence signals were measured in a microplate reader (Biotek Synergy 2); (vi) Leakage of cytoplasmic contents: The residual protein concentration in the captured sample can be measured with the Bradford assay (SK3041, Sangon Biotech, China); Chromosomal DNA was extracted using an Ezup Column Bacteria Genomic DNA Purification Kit (SK8255, Sangon Biotech), then verified by DNA agarose gel electrophoresis (0.6% agarose gel at 100 V for 30 min in 1 × TAE buffer); (vii) Concentration of persulfate was determined using a UV–Vis spectrophotometer (Lambda 25, Perkin Elmer Inc., USA) with a cuvette providing a light path of 10 mm. At each time interval, 1 mL sample was transferred to a 10 mL glass vial containing 9 mL distilled water, followed by adding 0.05 g $NaHCO_3$ and 1 g KI powder (Liang et al., 2008). The mixture was then hand shaken and set for equilibrium for 15 min before measuring the absorbance at 400 nm. The concentration of persulfate was calculated according to the calibration curve.

2.5. Chronoamperometry

NP (5 mg) were first dispersed in 20 μL of nafion perfluorinated resin solution (5 wt %, Aldrich) and 50 mL ethanol (99.9%, Aldrich). The mixture (5 μL) was dropped onto a ITO electrode and dried for 10 min; this procedure was repeated three times. The reactor contained a glassy carbon electrode, a coiled Pt wire, and an Ag/AgCl/KCl (sat) electrode as a working, counter, and reference electrode, respectively and 0.1 M phosphate buffer (pH ≈ 7) as an electrolyte. Chronoamperometries were carried out with an open circuit, and electrochemical measurements were subsequently added into the electrochemical working station at stated intervals with final concentrations of 0.5 mM PS and 7 $\log_{10}$ cfu/mL *E. coli* K-12 cells, respectively.

3. Results and discussions

3.1. Characterization of natural pyrrhotite

XRD pattern in Fig. 1a indicates the pristine natural pyrrhotite (NP) is composed of mixed phases of pyrrhotite-6T ($Fe_{1-x}S$, PDF 29-0725) and pyrite (FeS_2, PDF 42-1340) (Xia et al., 2015a), as NP always occurs with impurity mineral phases. SEM image in Fig. 1b indicates NP powders are in a heterogeneous size ranged from 10 to 30 μm and many mechanically ground fractures are observed on NP surface. The surface elements of NP were also analyzed by SEM-EDX (inset of Fig. 1b) and XPS (Fig. 1c). Both results confirmed the main existence of Fe, S and O of NP, and the estimated chemical formula of NP can be expressed as $FeS_{0.6}O_{0.52}$. The non-stoichiometric Fe to S ratio revealed vacancies were at the S sites in the crystal structure, mainly due to the oxidation of NP surface. Importantly, the 53.2% of Fe(II) on pristine NP surface (Fig. 1c) indicates its great potential for catalyzing PS to generate reactive species. Apart from Fe and S, Si, Al, K, Ca, Mg, Zn are also existed, based on the results of EMPA in Table S2. As shown in Fig. 1d, the magnetic loop indicates pristine NP possesses a saturation magnetization of 6 emu/g, with little coercivity (16 Oe) and remanence (0.056 emu/g). The soft magnetic property indicates NP can be magnetically recycling without great aggregation (Xia et al., 2016). As shown in Fig. S1, the NP powders can be immediately drawn to one side of the beaker when an external magnet was placed nearby, indicating its great potential for application.

3.2. E. coli inactivation by NP/PS system

3.2.1. Reactivity of natural pyrrhotite

The adsorption and inactivation profiles of *E. coli* K-12 against the reaction time in various situations are shown in Fig. 2a. The NP alone had no obvious adsorption toward *E. coli* K-12, as no cells' loss occurred within 30 min. Meanwhile, less than 0.2 $\log_{10}$ cfu/mL of cells' loss was noticed with PS alone, suggesting that the production of oxidizing radicals from PS alone was limited within 30 min. Impressively, a rapid decrease of the *E. coli* K-12 concentration was observed once the NP was involved, which exhibited a pseudo-first-order kinetics over exposure time with a rate constant of 0.34 1/min. Similarly, the Gram-positive bacteria of *S. aureus* with thicker cell envelope was found to exhibit similar inactivation kinetics with *E. coli* K-12 (Ng et al., 2016). This result evidenced that the combination of NP with PS can efficiently inactivate both types of cells.

In contrast with NP, the synthesized ZVI of nano-size was also utilized to catalyze PS for *E. coli* inactivation. Attributed to its large specific area, ZVI exhibited a better performance than NP, which can totally inactive 7 $\log_{10}$ cfu/mL of *E. coli* within 15 min (0.44 1/min, Fig. 2a). The results indicate the catalytic activity of NP is still not comparable with commercial ZVI. However, NP may still can work as an alternative material for PS activation, attributed to its merits like earth abundant and well enough catalytic activity.

To further evaluate the catalytic activity from leached ions of NP, the ions leaching in the NP/PS system was also monitored (Fig. S2). In the NP solution, which releases Fe^{2+} slowly and the observed aqueous concentration of total dissolved iron (9.96 mg/L) is comparable to the Fe^{2+} concentration (9.66 mg/L). In the NP/PS system, the total dissolved iron concentration gradually increases to 4.99 mg/L while Fe^{2+} are maintained at relatively low concentrations (0.4 mg/L). This suggests that the released Fe^{2+} could react with PS instantly and form Fe^{3+}. Notably, due to the fact that some of the Fe^{3+} could form $Fe(OH)_2$ or $Fe(OH)_3$ and precipitate, thereby the concentration of total soluble Fe amount was halved in the presence of PS. Similar observation was also obtained in other study

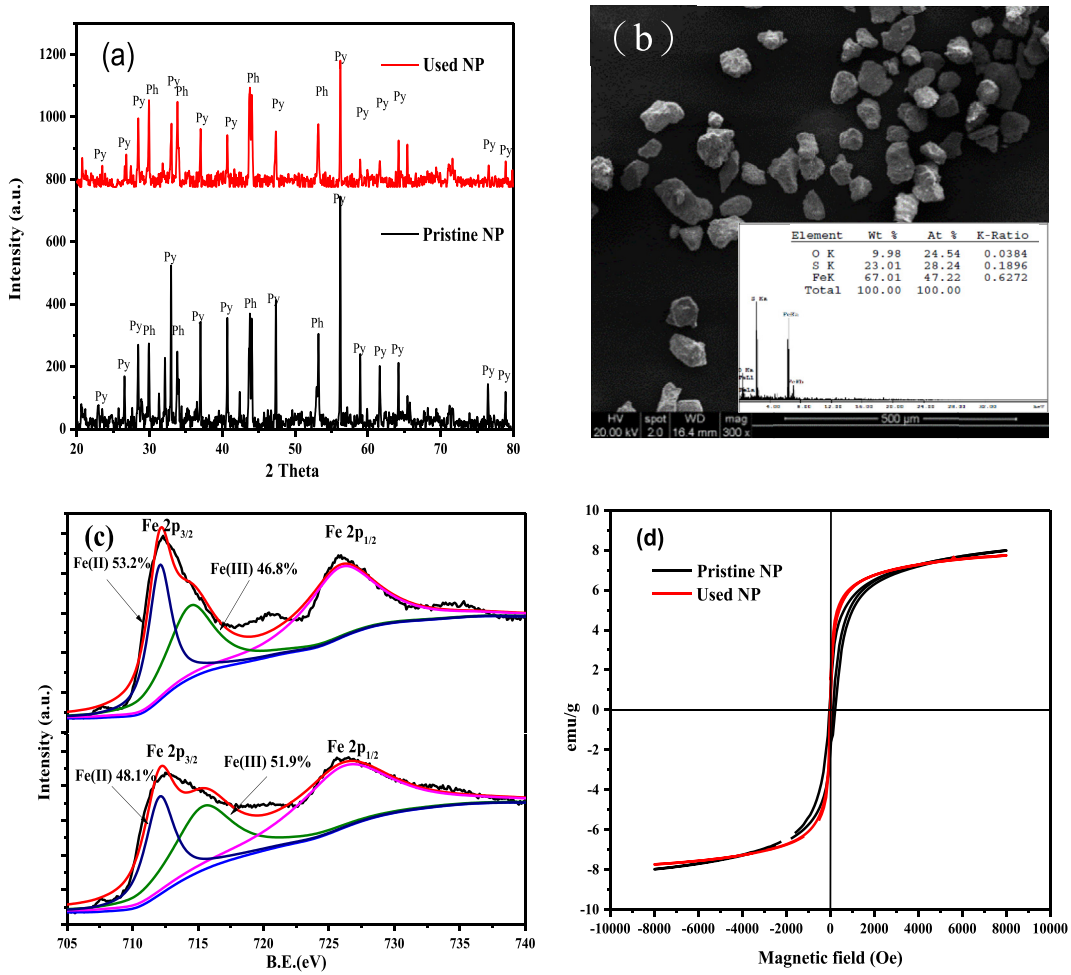

Fig. 1. (a) XRD, (b) SEM-EDX, (c) XPS spectra and (d) magnetic loops of pristine and recycled NP.

(Liang et al., 2010). It would be worthwhile observing that leached Fe (especially Fe^{2+}) might be problematic for some applications like wastewater treatment. Therefore, a further precipitation step may be needed to eliminate the dissolved Fe, which can be obtained by the addition of base like NaOH to form $Fe(OH)_3$. Meanwhile, equivalent amount of leaked Fe^{2+} (10 mg/L) or Fe^{3+} (10 mg/L) was respectively added to catalyze PS for *E. coli K-12* inactivation. As shown in Fig. 2a, due to the low concentration of Fe^{2+}, the Fe^{2+} was consumed quickly and can't trigger enough ROS to attack *E. coli*, thereby only a slight decrease of cell density was noticed. This result also suggests that the bacterial inactivation due to the Fe^{2+} ion-leaching induced homogeneous catalytic reactions was negligible when NP was used as catalysts.

The decomposition of PS by NP was also studied through measuring the residual persulfate anion ($S_2O_8^{2-}$). The added PS (0.5 mg/L) was sharply decomposed (60%) in the presence of NP, which followed a first-order kinetics' model (k = 0.021 1/min, Fig. 2b). Moreover, a notable observation was that the PS decay by NP was further enhanced by *E. coli*, indicating *E. coli* can accelerate the PS activation by NP. In contrast, no noticeable PS decomposition occurred when only *E. coli* added under the same conditions. Thus, it is concluded that the NP is efficient to activate the PS for inactivating *E. coli*.

3.2.2. *Effect of initial NP, E. coli K-12 and PS concentration*

First, *E. coli* K-12 inactivation was carried out to explore the effects of NP loading in the NP/PS system (Fig. 2c). An increase in NP loading had an obvious positive effect on *E. coli* inactivation when NP loading increased from 0.25 g/L to 1 g/L, with k value increased from 0.21 1/min to 0.34 1/min, respectively. When NP loading further increased to 1.25 g/L, a slight decline (0.32 1/min) in the *E. coli* inactivation efficiency was noticed, suggesting that the NP dose was the controlling factor of radicals' generation. This inhibition effect at 1.25 g/L of NP can be related to the scavenging effect of the NP, because radicals ($\cdot SO_4^-$) would be mainly generated by NP activation but they can also react with surface ≡Fe(II) on NP in a heterogeneous system. Similar results were also obtained in other work (Yan et al., 2011; Guan et al., 2013).

Insignificant difference in inactivation kinetics was observed for different initial *E. coli* K-12 concentrations ranging from 5 to 8 $\log_{10}$ cfu/mL (Fig. 2d), and the measured k value from three batch experiments can be described reasonably well by a similar k value (0.36, 0.34, 0.35 1/min, one way ANOVA, $p > 0.05$). The observed insensitivity to initial cell density is consistent with other disinfection processes like chlorine or ferrate (Luh and Marinas, 2007; Hu et al., 2012).

Fig. 2e presents the inactivation efficiencies of *E. coli* K-12 at a varying dosage of PS. The *E. coli* K-12 removal was enhanced with the PS concentration increased from 0.25 mM (0.12 1/min) to 1 mM (0.47 1/min), respectively. This increased inactivation efficiency was mainly resulted from the accelerated generation of radicals that occurred with higher doses of PS. Further increasing the PS

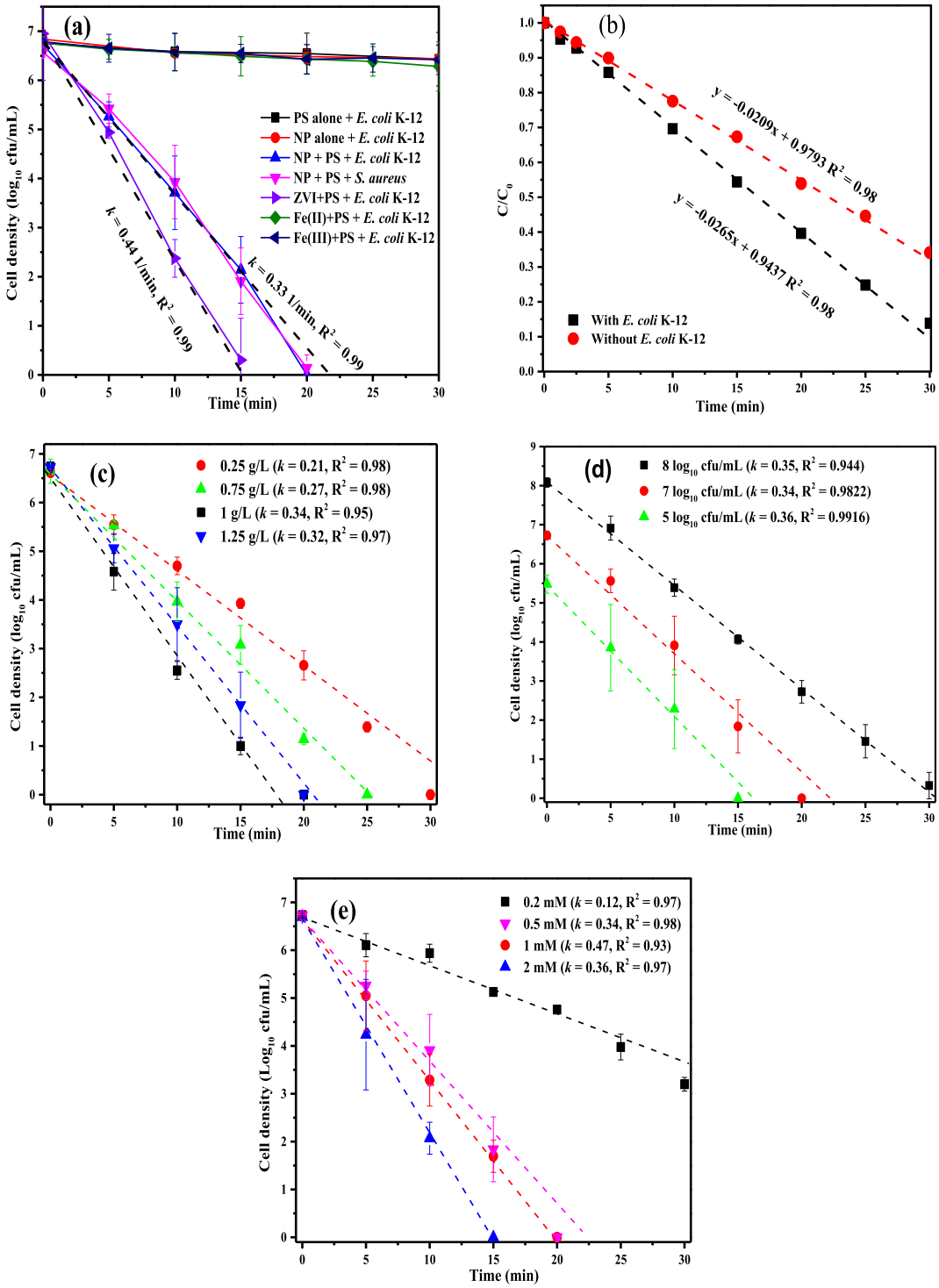

Fig. 2. (a) Sulfate radical-mediated bacterial inactivation in NP/PS system; (b) PS decomposition by NP with and without *E. coli* K-12; Influences of c) NP dose; d) cell density; e) PS concentration on bacterial inactivation by NP/PS system. Experimental conditions: [*E. coli* K-12] = 5-7 $\log_{10}$ cfu/mL, [*S. aureus*] = 7 $\log_{10}$ cfu/mL, [NP] = 0.5–1.25 g/L, [PS] = 0.5–2 mM.

concentration to 2 mM (0.36 1/min) did not enhance the inactivation efficiency but resulted in a slight inhibition, perhaps due to the quenching of $\cdot SO_4^-$ by surface Fe(II) of NP (Guan et al., 2013).

3.3. Reactive species and possible mechanism

Obviously, the good *E. coli* inactivation performance of NP/PS system was mainly attributed to the NP activated PS and its great generation of various reactive species. To analyze the presence and contributions of the specific reactive species, *E. coli* inactivation performance was thus examined by adding various scavengers in the NP/PS system, including methanol for $\cdot SO_4^-$, *tert*-butyl alcohol (TBA) for •OH, Fe(II)-EDTA for H_2O_2, TEMPOL for $\cdot O_2^-$ (Xia et al., 2013; Xia and Lo, 2016; Liu et al., 2014). In the control

experiment without PS, no significant cells' loss was observed by adding 2 mM of each scavenger, indicating no toxicity of these chemical scavengers to the *E. coli* within test time period (Fig. S3). First, the inhibition of *E. coli* K-12 inactivation was not accompanied by adding 2 mM TEMPOL, indicating the weak bactericidal contribution of $\cdot O_2^-$ (Fig. 3a). The is mainly due to the limited formation of $\cdot O_2^-$ in the NP/PS system, consistent with the result in Fig. S4a. Although O_2 is known to readily accept electron from transition metal to produce $\cdot O_2^-$, which is unstable and may readily converse into H_2O_2 or $\cdot SO_4^-$, thereby limited detection occurs in the present condition (Zhang et al., 2017). Second, the involvement of H_2O_2 was affirmed by the moderate decrease in the inactivation kinetics after adding 2 mM Fe(II)-EDTA (1.9 $\log_{10}$ cfu/mL of cells survived, Fig. 3a). Generally, when $Fe_{1-x}S$ is exposed to the air, H_2O_2 can be thermodynamically generated by either two electron reduction of surface-adsorbed O_2 from Fe(II) or disproportionate reaction of two $\cdot$OH (Liu et al., 2015; Fang et al., 2016). As show Fig. S4b, the great generation of H_2O_2 was accumulated to almost 5 μM without O_2 purging. Third, methanol and TBA were used to differentiate $\cdot SO_4^-$ from $\cdot$OH, because TBA without an alpha hydrogen was also readily reactive toward $\cdot$OH, but their reaction with $\cdot SO_4^-$ was over 1000-fold slower than methanol (Gao et al., 2016). Obviously, $\cdot SO_4^-$ played the leading role rather than $\cdot$OH was virtually observed, based on the more remarkable inhibition when 2 mM methanol added (5.5 $\log_{10}$ cfu/mL of cells survived, Fig. 3a) than that of 2 mM TBA (3.2 $\log_{10}$ cfu/mL of cells survived, Fig. 3a). Therefore, it can infer that $\cdot SO_4^-$ is mainly responsible for bacterial inactivation in the NP/PS system. Moreover, EPR results in Fig. 3b shows the obvious signals of both DMPO-$\cdot$OH (1:2:2:1) and DMPO-$\cdot SO_4^-$ (1:1:1:1:1:1), indicating large quantities of both $\cdot$OH and $\cdot SO_4^-$ radicals were generated immediately in the NP/PS system (Xiong et al., 2014). As identified above, all of the extracellular radicals $\cdot SO_4^-$, $\cdot$OH and H_2O_2 work collectively for the inactivation of *E. coli* K-12.

To analyze the interaction occurred on NP surface of NP/PS system, the *in situ* ATR-FTIR characterization was conducted and results were shown in Fig. 3c. After addition of PS, the FTIR spectrum of pristine NP showed an increased absorption at around 1273 1/min and 1046 1/min (the symmetric and asymmetric vibrations of S═O═S of sulfonate group), indicating the adsorptive interaction of PS occurred on NP surface (Lee et al., 2016). Meanwhile, the small band occurred at 1057 1/cm of pristine NP was blue shifted to 1079 1/cm after PS addition, suggesting the formation of a complex at NP surface. It is thus inferred that the interaction between Fe(II) and PS leads to the formation of a weak bond at the surface of NP like ≡Fe(II)···O_3SO—OSO_3 (eq (1)), based on Lei et al.'s work (2015). The weak bond of ≡Fe(II)···O_3SO—OSO_3 could trigger the broken of O—O bond, accompanied by the generation of ≡Fe(III) and $\cdot SO_4^-$ (eq (2)) (Duan et al., 2015, 2016). Meanwhile, the NP surface H_2O/—OH bond at 3100 1/cm became relatively invisible after PS addition, suggesting the complex and generated $\cdot SO_4^-$ may promote absorbed

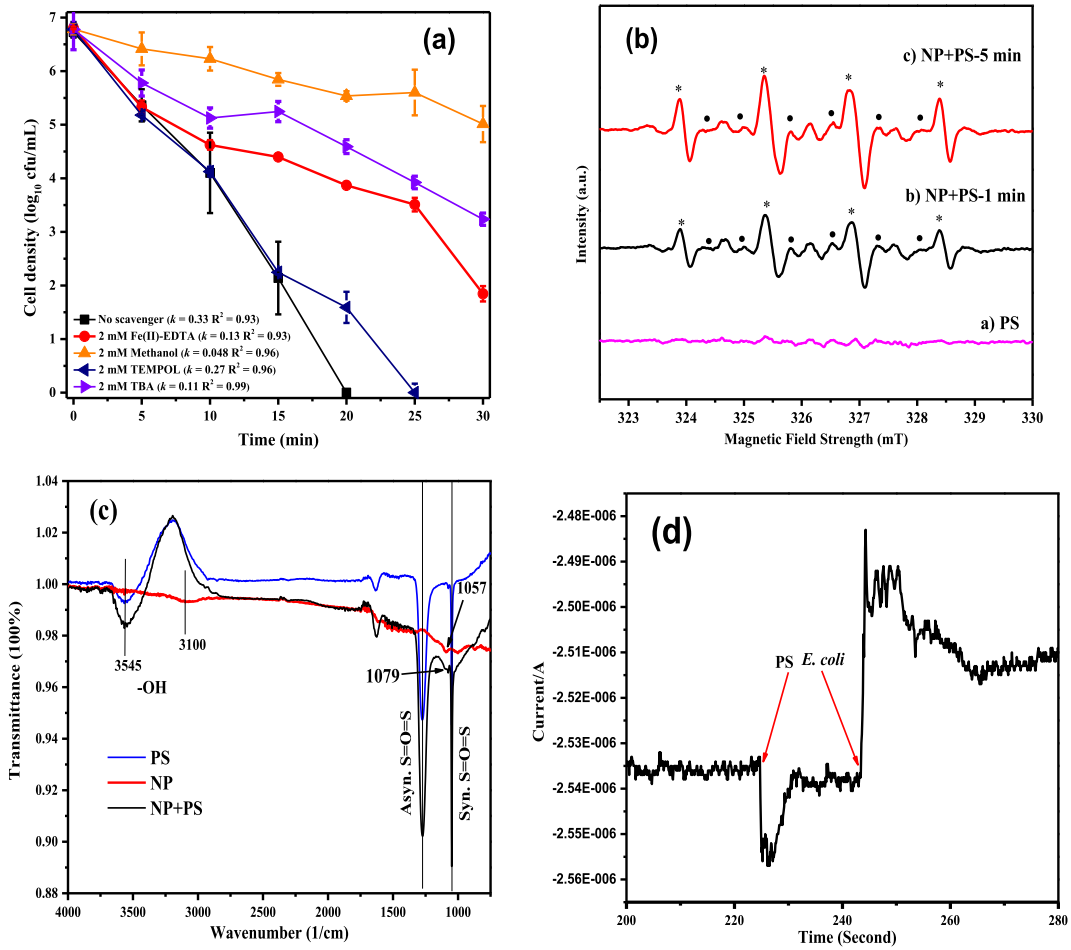

Fig. 3. (a) Scavenger quenching on bacterial inactivation by NP/PS system; (b) ESR spectra of DMPO spin-trapping adducts (asterisk represent DMPO-$\cdot$OH, and circle represent DMPO-$\cdot SO_4^{2-}$); (c) ATR-FTIR spectra of the PS solution alone, the NP in water, and the NP in PS solution; (d) Chronoamperometric measurements of NP electrode after adding PS and *E. coli* K-12 in turn. Experimental conditions: [*E. coli* K-12] = 7 $\log_{10}$ cfu/mL, [NP] = 1 g/L, [PS] = 0.5 mM.

H_2O/−OH to transform into •OH through eq (3), because $•SO_4^-$ possesses higher oxidative potential (2.5–3.1 V) than •OH (Gao et al., 2016). This was confirmed by the observation in Fig. 3b, the DMPO-$•SO_4^-$ signals diminished a little, accompanied by a slight increase in the DMPO-•OH signals from 1 min to 5 min in NP/PS system, indicating the DMPO-$•SO_4^-$ adduct can converse into DMPO-•OH adduct over time (Zhong et al., 2015). Subsequently, •OH may also thermodynamically form into H_2O_2 through disproportionated reaction (eq (4)) (Avetta et al., 2015; Liu et al., 2015).

$$\equiv Fe(II) + O_3SO - OSO_3^- \rightarrow \equiv Fe(III)\ldots O_3SO - OSO_3^- \quad (1)$$

$$\equiv Fe(II)\ldots O_3SO - OSO_3^- \rightarrow \equiv Fe(III) + •SO_4^- + SO_4^{2-} \quad (2)$$

$$•SO_4^- + H_2O/OH_- \rightarrow •OH + SO_4^{2-} \quad (3)$$

$$•OH + •OH \rightarrow H_2O_2 \quad (4)$$

To further analyze the complex and electron transfer, the current change toward the NP electrode was detected in the chronoamperometric measurements when PS and *E. coli* K-12 were added in turn (Fig. 3d). After the injection of PS, a small negative current peak was detected due to the instant electron movement from the NP electrode to PS, most likely through the formation of charge transfer complex ($\equiv Fe(II)\cdots O_3SO{-}OSO_3^-$). Subsequently, upon the addition of *E. coli* K-12, a slight positive current flow forms indicated electrons were transferred from *E. coli* K-12 to the NP/PS complex, likely due to the oxidation of bacterial cells occurred. In contrast, no current change occurred when *E. coli* K-12 was directly added on NP (Fig. S5), suggesting no electron transfer reaction happened without PS. Therefore, the PS activation by NP involved electron transfer from NP to PS, and *E. coli* inactivation involved electron transfer from *E. coli* to NP/PS complex, in which NP/PS complex engagement as a facile electron mediation was essential.

3.4. Influences of several factors to NP/PS system

3.4.1. Effect of temperature, pH, dissolved oxygen

Reaction temperature is a key operating factor in AOPs. Generally, increasing temperature can accelerate the decomposition rate of PS, thus increase the concentration of $•SO_4^-$, which also in turn facilitates the AOP reaction (Ji et al., 2015). Therefore, *E. coli* inactivation was examined within a temperature range of 20 °C–50 °C in NP/PS system. First, the results of control experiment at different temperature in Fig. S6a exhibited negligible loss of cells within 30 min, indicating the contribution to cells' loss from thermal activation of PS is limited within this time period. Although the thermal activation of PS to generate sulfate radicals was really occurred at higher temperature like 50 °C (Ji et al., 2015, 2016), some injured cells still can survive after cultivation because of the limited reaction time, thereby no significant loss of *E. coli* density can be observed. In fact, elevated temperature may still favor oxidative reactions based on thermodynamic law. As shown in Fig. 4a, the inactivation kinetics in NP/PS system are similar with the general trend, indicating higher temperature resulting in higher inactivation efficiency. The measured rate constant increased roughly 2-fold when temperature was increased from 20 °C (0.34 1/min) to 50 °C (0.69 1/min). On the basis of this trend, it might be deduced that PS activation process by NP is endothermic: higher temperature would shift the equilibrium to produce more reactive species and thus improve the bacterial inactivation efficiency (Feng et al., 2016).

Inactivation kinetics (Fig. 4b) in NP/PS system was found to be highly dependent on pH, lower pH can obtain a higher inactivation performance. The control experiments with PS alone at different pH was also conducted, and no significant *E. coli*' loss occurred within 20 min, indicating the pH has no obvious effect on cells' viability (Fig. S6b). In general, $•SO_4^-$ based AOP can achieve a higher oxidative activity at higher pH, due to the $•SO_4^-$ could provoke an accelerated PS decomposition and transformation reactions generating additional •OH under alkaline condition (Lei et al., 2015; Neta et al., 1988). However, PS solution with a pH 3.0 (0.68 1/min) demonstrated the best inactivation performance, and a >1.5-fold decline was observed at pH 5.0 (0.45 1/min). When pH was increased from 7 (0.30 1/min) to 9 (0.17 1/min), the inactivation kinetics were observed to decrease roughly 1.7-fold. To analyze the pH effect, the surface charge of NP and *E. coli* have been detected at different pH conditions. As shown in Fig. S7, the zero charge of NP is 4.6, while *E. coli* exists predominantly in its deprotonated form at pH 3.0–11.0. Therefore, the high inactivation efficiency at acidic condition (pH 3, 5) can be attributed to the electrostatic adsorption, while the low inactivation at pH 9, 11 was probably in part due to the electrostatic repulsion between the deprotonated *E. coli* and NP, because almost all of the cells had a negative charge under such conditions (Fig. S7). Moreover, at alkaline condition, the oxidized Fe^{3+} ions may form oxyhydroxides like $FeOH^{2+}$/$Fe_2(OH)_2^+$/$Fe(OH)_3$ to precipitate on the surface of NP, which covered the surface reactive sites of NP and caused inhibition for activating PS to form $•SO_4^-$ (Zhang et al., 2017). Notably, the pH variation in NP/PS system was also monitored at five initial pH, all the pH values were decreased a little and rapidly to a specific pH value (Fig. S8), this is mainly due to the partial dissolution of $Fe_{1-x}S$ in the water (Liu et al., 2015). Since the pH was rapidly attained to an equilibrium, and no significant cells' loss was observed with NP alone/PS alone and even in the pH controlled solution, it is reasonable to indicate that the *E. coli* inactivation by dissolved NP induced pH interference may not that significant. Therefore, the inactivation kinetics revealed that the bacterial inactivation process was more favorable in acidic and mild alkaline conditions.

Dissolved O_2 has an impact on PS activation as O_2 is an electron acceptor. As shown in Fig. 4c, the total inactivation of 7 $\log_{10}$ cfu/mL of *E. coli* was obtained at 15 min with air purging (0.46 1/min) and 20 min without air purging (0.34 1/min), while only 4.6 $\log_{10}$ cfu/mL of *E. coli* was obtained at 20 min under N_2 purging (0.23 1/min). When Fe(II) is exposed to the air, molecular O_2 could be reduced to $•O_2^-$ or H_2O_2 directly by Fe(II) via single- or two-electron transfer routes (Harrington et al., 2012; Jones et al., 2013), which would accelerate the PS activation to produce $•SO_4^-$ (Zhang et al., 2017) (eqs. (5)–(8)). To test the effects of dissolved O_2, the generated $•O_2^-$ and H_2O_2 concentrations were determined. Results in Fig. S4a present the little formation of $•O_2^-$ (no NBT transformation occurred at three conditions), while H_2O_2 concentration increased in the order of N_2 purging-pyrite system (3 μM) > no purging pyrite system (4.995 μM) > air purging-pyrite system (5.65 μM) (Fig. S4b). Therefore, increasing O_2 concentration could lead to the generation of more H_2O_2, thus to trigger more generation of $•SO_4^-$, collectively resulting in a higher inactivation efficiency.

$$Fe(II) + O_2 \rightarrow •O_2^- + Fe(III) \quad (5)$$

$$2Fe(II) + O_2 + 2H^+ \rightarrow H_2O_2 + 2Fe(III) \quad (6)$$

$$S_2O_8^{2-} + •O_2^- \rightarrow •SO_4^- + SO_4^{2-} + O_2 \quad (7)$$

$$S_2O_8^{2-} + 2H_2O_2 \rightarrow 2•SO_4^- + 2H_2O + O_2 \quad (8)$$

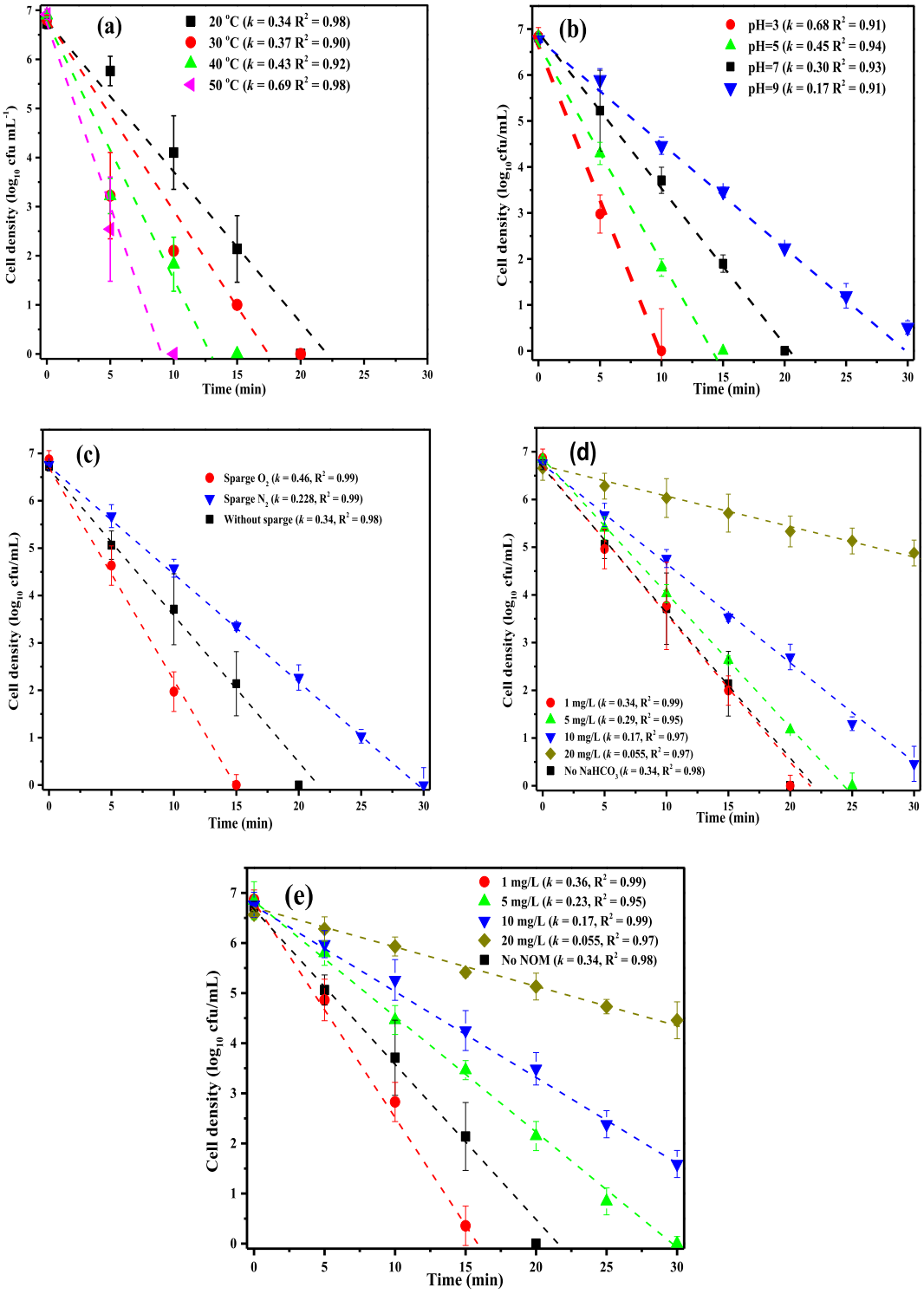

Fig. 4. Influence of a) temperature; b) initial pH; c) dissolved O_2; d) $NaHCO_3$; e) natural organic matter on bacterial inactivation by NP/PS system. Experimental conditions: [*E. coli* K-12] = 7 $\log_{10}$ cfu/mL, [NP] = 1 g/L, [PS] = 0.5 mM.

3.4.2. *Effect of bicarbonate, NOM*

Bicarbonate was the representative of inorganic carbon existed in natural water at the range of 0.1–50 mg/L, which can quench radicals to inhibit oxidation process (Wu et al., 2015). As shown in Fig. 4d, a $NaHCO_3$ concentration to 1 mg/L (0.34 1/min) exhibited similar inactivation kinetics with that of no $NaHCO_3$ addition (0.34 1/min); with further addition of $NaHCO_3$, the inactivation efficiency decreased significantly (one way ANOVA, $p < 0.05$) in the presence of 5 mg/L $NaHCO_3$ (0.29 1/min) and almost totally inhibited when 20 mg/L $NaHCO_3$ (0.055 1/min) were added. Wu et al. (2015) suggested that bicarbonate could form complexes on catalyst surface and even quench the $\cdot SO_4^{2-}$ to generate the $\cdot CO_3^-$. The great consumption of $\cdot SO_4^{2-}$ and the relative lower reactivity of $\cdot CO_3^-$ (2.09 eV) than $\cdot SO_4^{2-}$ (2.5–3.1 eV, Zhao et al., 2010) would cause the

detrimental effect to NP/PS system, thus to greatly inhibit *E. coli* K-12 inactivation.

Similarly, natural organic matter (NOM) is usually present in the aquatic environment, which can act as radical scavenger via competing for •OH and $•SO_4^-$. As shown in Fig. 4e, *E. coli* inactivation rate was firstly promoted to 0.36 1/min with the addition of 1 mg/L NOM, in contrast with free NOM (0.34 1/min). In fact, hydroquinones, quinones and phenols in NOM can form into semiquinone radicals, which might stimulate the decomposition of PS into •OH and $•SO_4^-$, similar to the way of reducing H_2O_2 to •OH, thus to accelerate the AOP process (De Laat et al., 2011). However, the *E. coli* inactivation rate then decreased significantly from 0.23 1/min to 0.055 1/min when NOM further increased from 5 mg/L to 20 mg/L, indicating the stimulated effect of NOM was overwhelmed by its detrimental effect. Michael-Kordatou et al. (2015b) suggested that NOM contains many phenolic hydroxyl and carboxyl groups, which can be adsorbed onto catalyst surface and block reactive sites, thus to inhibit the oxidation process.

3.5. Cell destruction process

The bacterial envelope, composed of outer membrane, peptidoglycan layer, and cytoplasmic membrane, always worked as the first target of being exposed to ROS attack (Xia et al., 2016). First, the BacLight kit fluorescent microscopic method was utilized to directly observe the permeability changes of cell envelop in the NP/PS system. As shown in Fig. 5a, the viable cells were with intense green fluorescence. After being treated for 10 min, most cells turned to red fluorescence, indicating most cells were disrupted and intracellular components were stained. With prolonged treatment to 20 min, all the images were in red, indicating cells' envelope were all broken with more red stained intracellular components. Similarly, compared with the SEM image of initial intact *E. coli* K-12 cells (0 min) in Fig. 5b, the treated cell envelope was deformed after 20 min treatment. Actually, the cell envelope contains essential protein components such as respiratory chain, which generate energy (ATP) with functionalized electron chains, playing a vital role in bacterial metabolism (Bosshard et al., 2010).

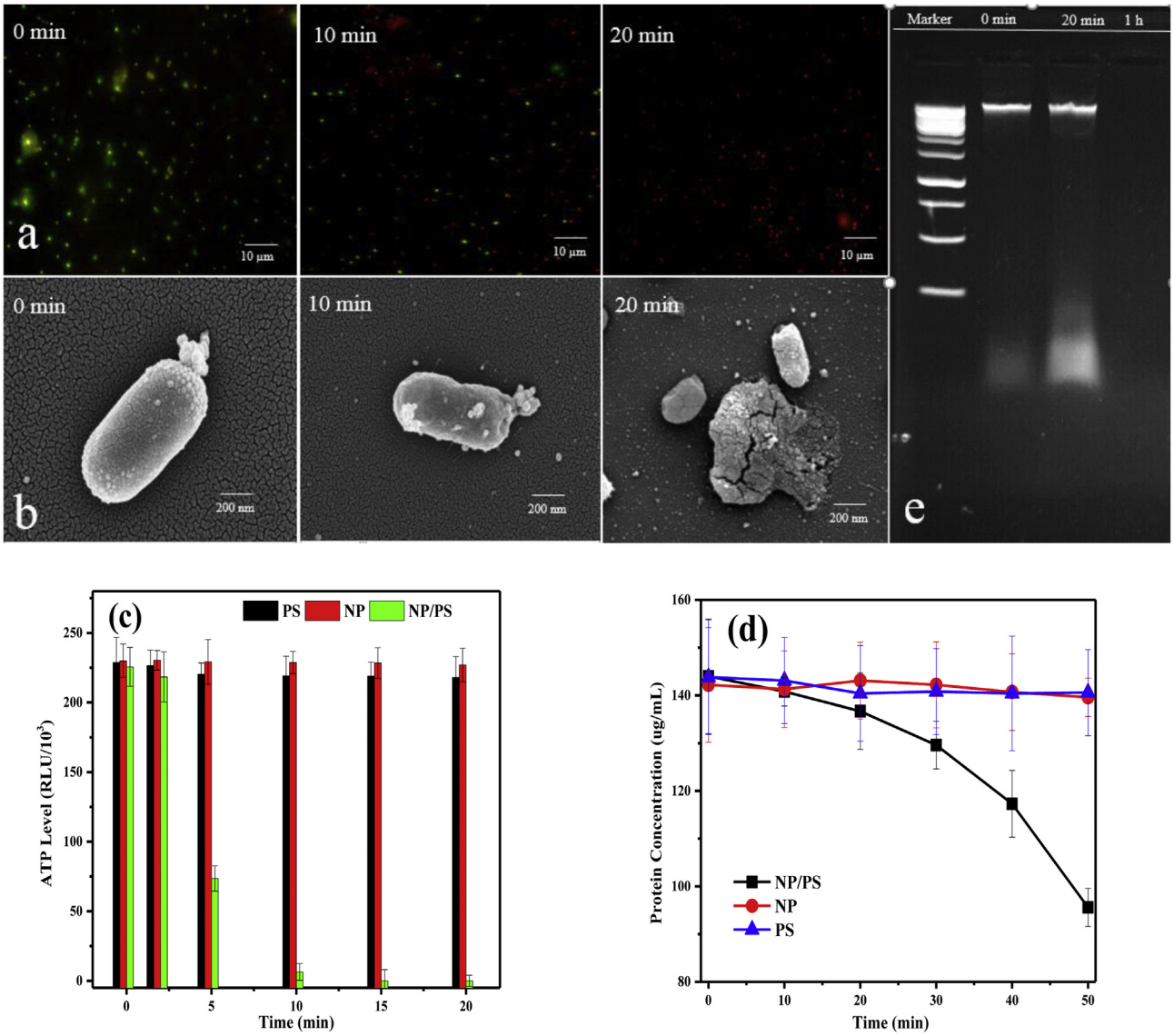

Fig. 5. (a) Fluorescence microscopic images of *E. coli* K-12; (b) SEM images of *E. coli* K-12; (c) ATP content in cells (note: RLU denotes the relative luminescence unit); (d) Detection of protein concentration in 100 μL concentrated cell lysate from 10 mL bacterial suspension (e) leakage and destruction of bacterial genomic DNA extracted from harvested cells during treatment by NP/PS system. Experimental conditions: [*E. coli* K-12] = 7 $\log_{10}$ cfu/mL, [NP] = 1 g/L, [PS] = 0.5 mM.

Associated with the damaged envelope, the cells were almost instantaneously inactivated by metabolic arrest as a consequence of a drastic drop in the ATP level within initial 10 min treatment (Fig. 5c). Generally, ROS has been found to inhibit ATP formation either by behaving like a protonophore or by inhibiting enzymes in the respiratory chain to dissipate the proton motive force (Parker et al., 2014).

After the penetration of cell envelope, the ROS can subsequently injure the cells by reacting with various biomolecules, such as cytoplasmic protein and genome (Sun et al., 2014). As shown in Fig. 5d, the protein content of treated cells (10 mL) in Bradford assay was maintained at around 142 mg/mL within the initial 10 min but then decreased a little to 136.7 mg/mL at 20 min, assumed to be indicative of starting peroxidation of protein during treatment. The destruction of genomic DNA could be observed in Fig. 5e because the fluorescent intensity of the DNA bands started to fade around 20 min and then totally disappeared with prolonged to 1 h. Damage to *E. coli*'s genome is lethal to the cells, which could efficiently disrupt events instrumental to the bacterial life cycle. Or else cells in a viable but non-culturable state may still survive to cause the health risks in water (Zhang et al., 2015). These results revealed that the cell envelope of *E. coli* K-12 was firstly decomposed, then cytoplasmic components leaked and degraded, finally resulting in the cells' mineralization.

3.6. Stability and recycle of NP

The stability of NP was investigated by repeating *E. coli* inactivation experiments with recycled NP. After each experiment, NP was magnetically captured on the bottom of flask and the supernatant was poured out, then *E. coli* K-12 cells and PS solution were added to start the next run. After four times' recycling, the *E. coli* K-12 inactivation efficiency decreased with about 4 $\log_{10}$ cfu/mL cells' inactivation (Fig. 6a), which was likely due to the loss of active sites on the NP surfaces, including oxidation of surface Fe(II) and adsorption of *E. coli* oxidation products. XPS results (Fig. 1c) confirmed that the atomic ratio of ≡Fe(II)/≡Fe(III) was decreased from 1.14 (53.2%/46.8%) for pristine NP to 0.93 (48.1%/51.9%) for used NP, thus resulting in a decreased performance. Meanwhile, FTIR analysis (Fig. S9) also show that out-of-plane was bend of amide A (3274 1/min) and amide B (3060 1/min) groups of *E. coli* after treatment, which inhibit the surface Fe(II) to contact with PS (Xia et al., 2013). The semi-quantitative analysis of XRD pattern (Fig. 1a) showed that the ratio of py/ph decreased from 745/370 (2.01) to 405/318 (1.27), which may suggest the partial crystalline change from py to ph after reaction. However, no significant difference was observed in the saturated magnetism between fresh and recycled NP (Fig. 1a, d), indicating the magnetism of NP were still maintained even after 4 runs' test. After the fourth run, the recovered NP was washed by ultrapure water and dried for the fifth run. The *E. coli* inactivation efficiency almost recovered to that of initial run (Fig. 6a). This is mainly due to the cellular debris were removed from NP after wash treatment, as the characteristic peaks of organic functional groups greatly weakened (Fig. S9).

3.7. Environmental implications for authentic water treatments

As a preliminary step in investigating the potential application of NP/PS system, the inactivation experiments were thus conducted under authentic matrices of surface water (SW) and secondary wastewater effluents (WW). In contrast with that of ultrapure water (UPW), the inactivation kinetics in SW and WW decreased significantly, with the order of: UPW > SW > WW (Fig. S10). Based on the water parameters in Table S1, it can conclude that the slowed performances in SW and WW, were mainly caused by the natural water components like natural organic matter (TOC represents NOM) and inorganic ions (bicarbonate). $\cdot SO_4^-$ can react selectively against the prevailed nitrogen-containing organics in NOM through an electron transfer oxidation mechanism, thus the SW (TOC = 0.72 mg C/L) and WW (TOC = 5.4 mg C/L) are suspected to have a high $\cdot SO_4^-$ reactivity hindering the bacterial inactivation (Avetta et al., 2015). Meanwhile, part of $\cdot SO_4^-$ may complex or react with CO_3^{2-} present in the SW (bicarbonate = 6 mg/L) and WW (bicarbonate = 12 mg/L), also can greatly inhibit bacterial inactivation (Michael-Kordatou et al., 2015b). Moreover, both water matrices are at alkaline conditions (pH 8.3 of SW and pH 7.64 of WW) may also inhibit the inactivation efficiency to some content, based on the study of pH effect in Fig. 4b.

When the PS amount increased to 1 mM, NP/PS can totally inactivate the cells within 25 min in SW; while 3.5 $\log_{10}$ cfu/mL of *E. coli* still survive within 30 min in WW (Fig. S10). Further increase the PS amount to 2 mM, there are 2 $\log_{10}$ cfu/mL of *E. coli* still survive in WW (Fig. S10). Obviously, the inactivation efficiency was greatly enhanced with the increase amount of PS in both water matrices. The higher the concentration of PS, the more PS anions can be activated by NP, together with more sulfate radicals and

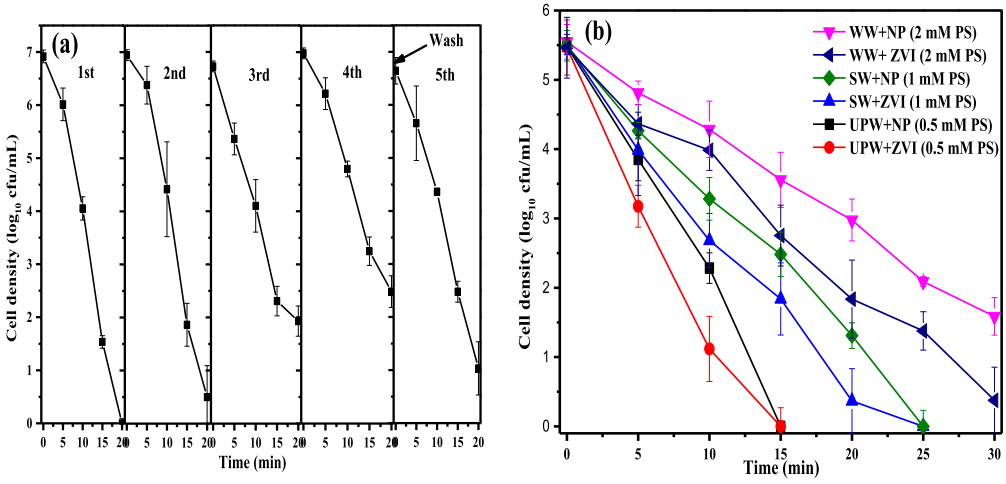

Fig. 6. a) repetitive use of recycled NP for *E. coli* K-12 inactivation; b) inactivation performance in different water matrix with NP/PS and ZVI/PS system. Experimental conditions: [*E. coli* K-12] = 7 $\log_{10}$ cfu/mL, [NP] = 1 g/L, [PS] = 0.5 mM.

derived ROS to inactivate cells (Feng et al., 2016). Based on the results, the selected suitable amount of PS was 1 mM for SW and 2 mM for WW, respectively.

In contrast, ZVI was also utilized to activate the selected amount of PS for *E. coli* inactivation, which exhibiting a slightly higher performance than that of NP/PS system in both UPW and authentic water matrices (Fig. 6b). This is probably occurred, because ZVI can accelerate the Fe(III)–Fe(II) cycle, thus to accelerate the PS activation (Liang et al., 2010). Meanwhile, ZVI also can react with dissolved oxygen to generate $\cdot O_2^-$ and a series of other ROS to further enhance the inactivation efficiency (Zhong et al., 2015). Although the catalytic activity of NP is still not comparable with commercial ZVI in different water matrices, NP still can be utilized as a cost-effective alternative material for application, attributed to its merits like earth abundant, good catalytic activity, and easy recyclable. In the framework of implementing safe wastewater reuse schemes, other technological parameters like reactor size, stirring velocity, etc., should be further optimized to meet the current challenges associated with hazardous bacteria spread into the environment.

4. Conclusions

Natural occurring pyrrhotite exhibited a notable catalytic activity to PS for *E. coli* inactivation. *E. coli* inactivation by NP/PS was enhanced with the increase of PS and NP doses at respective range of 0.2–1.0 mM and 0.15–1.0 g/L. It showed an independence on initial cell density, but greatly dependent on acidic pH and dissolved O_2. NOM stimulated *E. coli* inactivation at the concentration of 1 mM but inhibited at 5–20 mg/L. Bicarbonate inhibited the *E. coli* inactivation at the range of 0.1–2.0 mg/L. The bactericidal role of generated ROS was identified to be $\cdot SO_4^- > \cdot OH > H_2O_2$. The surface complex of NP played an important role in the generation of radicals from NP/PS. Catalytic oxidation of *E. coli* by NP/PS was also effective under the backgrounds of investigated actual waters, which provide a reference for application.

Acknowledgement

The project was supported by a research grant (GRF14100115) of the Research Grant Council, Hong Kong SAR Government and the Technology and Business Development Fund (TBF15SCI008) of The Chinese University of Hong Kong to P.K. Wong, and the research grants (41573086, 41425015 and 41603097) of National Science Foundation of China to Dr. G.Y. Li, T.C. An, D.H. Xia, respectively. P.K. Wong was also supported by CAS/SAFEA International Partnership Program for Creative Research Teams of Chinese Academy of Sciences.

The Supporting Information included the authentic water parameters, iron leakage, FTIR of used NP, Chronoamperometric measurements of NP electrode.

Appendix A. Supplementary data

Supplementary data related to this article can be found at http://dx.doi.org/10.1016/j.watres.2017.01.052.

References

Ahn, S., Peterson, T.D., Righter, J., Miles, D.M., Tratnyek, P.G., 2013. Disinfection of ballast water with iron activated persulfate. Environ. Sci. Technol. 47, 11717–11725.

Anastasi, E.M., Wohlsen, T.D., Stratton, H.M., Katouli, M., 2013. Survival of Escherichia coli in two sewage treatment plants using UV irradiation and chlorination for disinfection. Water Res. 47, 6670–6679.

Anipsitakis, G.P., Tufano, T.P., Dionysiou, D.D., 2008. Chemical and microbial decontamination of pool water using activated potassium peroxymonosulfate. Water Res. 42, 2899–2910.

Avetta, P., Pensato, A., Minella, M., Malandrino, M., Maurino, V., Minero, C., Hanna, K., Vione, D., 2015. Activation of persulfate by irradiated magnetite: implications for the degradation of phenol under heterogeneous photo-Fenton-like conditions. Environ. Sci. Technol. 49, 1043–1050.

Bosshard, F., Bucheli, M., Meur, Y., Egli, T., 2010. The respiratory chain is the cell's Achilles' heel during UVA inactivation in *Escherichia coli*. Microbiology 156 (7), 2006–2015.

Chesney, A.R., Booth, C.J., Lietz, C.B., Li, L., Pedersen, J.A., 2016. Peroxymonosulfate rapidly inactivates the disease-associated prion protein. Environ. Sci. Technol. 50, 7095–7105.

De Laat, J., Dao, Y.H., Hamdi El Najjar, N., Daou, C., 2011. Effect of some parameters on the rate of the catalysed decomposition of hydrogen peroxide by iron(III)-nitrilotriacetate in water. Water Res. 45 (17), 5654–5664.

Dobrowsky, P.H., De Kwaadsteniet, M., Cloete, T.E., Khan, W., 2014. Distribution of indigenous bacterial pathogens and potential pathogens associated with roof harvested rainwater. Appl. Environ. Microbiol. 80, 2307–2316.

Drzewicz, P., Perez-Estrada, L., Alpatova, A., Martin, J.W., Gamal El-Din, M., 2012. Impact of peroxydisulfate in the presence of zero valent iron on the oxidation of cyclohexanoic acid and naphthenic acids from oil sands process-affected water intermediates and reaction pathways from the degradation of microcystin-LR with sulfate radicals. Environ. Sci. Technol. 46, 8984–8991.

Duan, X., Su, C., Zhou, L., Sun, H., Suvorova, A., Odedairo, T., Zhu, Z., Shao, Z., Wang, S., 2016. Surface controlled generation of reactive radicals from persulfate by carbocatalysis on nanodiamonds. Appl. Catal. B Environ. 194, 7–15.

Duan, X., Sun, H., Kang, J., Wang, Y., Indrawirawan, S., Wang, S., 2015. Insights into heterogeneous catalysis of persulfate activation on dimensional-structured nanocarbons. ACS Catal. 5, 4629–4636.

Eischeid, A.C., Thurston, J.A., Linden, K.G., 2011. UV disinfection of adenovirus: present state of the research and future directions. Crit. Rev. Environ. Sci. Technol. 41, 1375–1396.

Fang, G.-D., Dionysiou, D.D., Al-Abed, S.R., Zhou, D.-M., 2016. Superoxide radical driving the activation of persulfate by magnetite nanoparticles: implications for the degradation of PCBs. Appl. Catal. B Environ. 194, 7–15.

Feng, Y., Wu, D., Deng, Y., Zhang, T., Shih, K.M., 2016. Sulfate radical-mediated degradation of sulfadiazine by $CuFeO_2$ rhombohedral crystal-catalyzed peroxymonosulfate: synergistic effects and mechanisms. Environ. Sci. Technol. 50, 3119–3127.

Gao, Y., Zhang, Z., Li, S., Liu, J., Yao, L., Li, Y., Zhang, H., 2016. Insights into the mechanism of heterogeneous activation of persulfate with a clay/iron-based catalyst under visible LED light irradiation. Appl. Catal. B Environ. 185, 22–30.

Guan, Y.H., Ma, J., Li, X.C., Fang, J.Y., Chen, L.W., 2011. Influence of pH on the formation of sulfate and hydroxyl radicals in the UV/peroxymonosulfate system. Environ. Sci. Technol. 45, 9308–9314.

Guan, Y., Ma, J., Ren, Y., Liu, Y., Xiao, J., Lin, L., Zhang, C., 2013. Efficient degradation of atrazine by magnetic porous copper ferrite catalyzed peroxymonosulfate oxidation via the formation of hydroxyl and sulfate radicals. Water Res. 47, 5431–5438.

Haaken, D., Dittmar, T., Schmalz, V., Worch, E., 2014. Disinfection of biologically treated wastewater and prevention of biofouling by UV/electrolysis hybrid technology: influence factors and limits for domestic wastewater reuse. Water Res. 52, 20–28.

Harrington, A.D., Hylton, S., Schoonen, M.A.A., 2012. Pyrite-driven reactive Oxygen species formation in simulated lung fluid: implications for coal workers' pneumoconiosis. Environ. Geochem. Health 34, 527–538.

Hu, L., Page, M.A., Sigstam, T., Kohn, T., Marinas, B.J., Strathmann, T.J., 2012. Inactivation of bacteriophage MS2 with potassium Ferrate(VI). Environ. Sci. Technol. 46, 12079–12087.

Huang, G., Ng, T.W., An, T., Li, G., Xia, D., Yip, H.Y., Zhao, H., Wong, P.K., 2017. Probing the intracellular organic matters released from the photocatalytic inactivation of bacteria using fractionation procedure and excitation-emission-matrix fluorescence. Water Res. 110, 270–280.

Ji, Y., Fan, Y., Liu, K., Kong, D., Lu, J., 2015. Thermo activated persulfate oxidation of antibiotic sulfamethoxazole and structurally related compounds. Water Res. 87, 1–9.

Ji, Y., Shi, Y., Dong, W., Wen, X., Jiang, M., Lu, J., 2016. Thermo-activated persulfate oxidation system for tetracycline antibiotics degradation in aqueous solution. Chem. Eng. J. 298, 225–233.

Johnson, R.L., Tratnyek, P.G., Johnson, R.O.B., 2008. Persulfate persistence under thermal activation conditions. Environ. Sci. Technol. 42, 9350–9356.

Jones, G.C., van Hille, R.P., Harrison, S.T.L., 2013. Reactive oxygen species generated in the presence of fine pyrite particles and its implication in thermophilic mineral bioleaching. Appl. Microbiol. Biotechnol. 97, 2735–2742.

Lee, H., Kim, H., Weon, S., Choi, W., Hwang, Y.S., Seo, J., Lee, C., Kim, J.-H., 2016. Activation of persulfates by graphitized nanodiamonds for removal of organic compounds. Environ. Sci. Technol. 50 (18), 10134–10142.

Lei, Y., Chen, C.-S., Tu, Y.-J., Huang, Y.-H., Zhang, H., 2015. Heterogeneous degradation of organic pollutants by persulfate activated by CuO-Fe_3O_4: mechanism, stability, and effects of pH and bicarbonate ions. Environ. Sci. Technol. 49, 6838–6845.

Liang, C., Guo, Y.Y., Chien, Y.C., Wu, Y.J., 2010. Oxidative Degradation of MTBE by Pyrite-activated Persulfate: Proposed Reaction Pathways, vol. 49, pp. 8858–8864.

Liang, C., Huang, C.F., Mohanty, N., Kurakalva, R.M., 2008. A rapid

spectrophotometric determination of persulfate anion in ISCO. Chemosphere 73, 1540–1543.
Liu, H., Bruton, T.A., Doyle, F.M., Sedlak, D.L., 2014. In situ chemical oxidation of contaminated groundwater by persulfate: decomposition by Fe(III)- and Mn(IV)-containing oxides and aquifer materials. Environ. Sci. Technol. 48, 10330–10336.
Liu, W., Wang, Y., Ai, Z., Zhang, L., 2015. Hydrothermal synthesis of FeS_2 as a high-efficiency Fenton reagent to degrade alachlor via superoxide-mediated Fe(II)/Fe(III) cycle. ACS Appl. Mater. Interfaces 7 (51), 28534–28544.
Luh, J., Marinas, B.J., 2007. Inactivation of Mycobacterium avium with free chlorine. Environ. Sci. Technol. 41 (14), 5096–5102.
Matzek, L.W., Carter, K.E., 2016. Activated persulfate for organic chemical degradation: a review. Chemosphere 151, 178–188.
Michael-Kordatou, I., Iacovou, M., Frontistis, Z., Hapeshi, E., Dionysiou, D.D., Fatta-Kassinos, D., 2015a. Erythromycin oxidation and ERY-resistant *Escherichia coli* inactivation in urban wastewater by sulfate radical-based oxidation process under UV-C irradiation. Water Res. 85, 346–358.
Michael-Kordatou, C., Michael, X., Duan, X., He, D., Dionysiou, M.A., Mills, Fatta-Kassinos, D., 2015b. Effluent organic matter: characteristics and potential implications in wastewater treatment and reuse applications. Water Res. 77, 213–248.
Neta, P., Huie, R.E., Ross, A.B., 1988. Rate constants for reactions of inorganic radicals in aqueous solution. J. Phys. Chem. Ref. Data 17 (3), 1027–1284.
Ng, T.W., Zhang, L., Liu, J., Huang, G., Wang, W., Wong, P.K., 2016. Visible-light-driven photocatalytic inactivation of *Escherichia coli* by magnetic Fe_2O_3-AgBr. Water Res. 90, 111–118.
Oh, W.-D., Dong, Z., Lim, T.-T., 2016. Generation of sulfate radical through heterogeneous catalysis for organic contaminants removal: current development, challenges and prospects. Appl. Catal. B Environ. 194, 169–201.
Parker, K.M., Zeng, T., Harkness, J., Vengosh, A., Mitch, W.A., 2014. Enhanced formation of disinfection byproducts in shale gas wastewater-impacted drinking water supplies. Environ. Sci. Technol. 48, 11161–11169.
Ren, Y., Lin, L., Ma, J., Yang, J., Feng, J., Fan, Z., 2015. Sulfate radicals induced from peroxymonosulfate by magnetic ferrospinel MFe2O4 (M = Co, Cu, Mn and Zn) as heterogeneous catalysts in the water. Appl. Catal. B Environ. 165, 572–578.
Rietveld, L.C., Norton-Brandao, D., Shang, R., van Agtmaal, J., van Lier, J.B., 2011. Possibilities for reuse of treated domestic wastewater in The Netherlands. Water Sci. Technol. 64, 1540–1546.
Rizzo, L., Manaia, C., Merlin, C., Schwartz, T., Dagot, C., Ploy, M., Michael, I., Fatta-Kassinos, D., 2013a. Urban wastewater treatment plants as hotspots for antibiotic resistant bacteria and genes spread into the environment: a review. Sci. Total Environ. 447, 345–360.
Rizzo, L., Fiorentino, A., Anselmo, A., 2013b. Advanced treatment of urban wastewater by UV radiation: effect on antibiotics and antibiotic-resistant *E. coli* strains. Chemosphere 92, 171–176.
Sharma, V.K., Zboril, R., McDonald, T.J., 2014. Formation and toxicity of brominated disinfection byproducts during chlorination and chloramination of water: a review. J. Environ. Sci. Health B 49, 212–228.
Soller, J.A., Schoen, M.E., Varghese, A., Ichida, A.M., Boehm, A.B., Eftim, S., Ashbolt, N.J., Ravenscroft, J.E., 2014. Human health risk implications of multiple sources of faecal indicator bacteria in a recreational waterbody. Water Res. 66, 254–264.
Sun, H.W., Li, G.Y., Nie, X., Shi, H.X., Wong, P.K., Zhao, H.J., An, T.C., 2014. Systematic approach to in-depth understanding of photoelectrocatalytic bacterial inactivation mechanisms by tracking the decomposed building blocks. Environ. Sci. Technol. 48, 9412–9419.
Teel, A.L., Ahmad, M., Watts, R.J., 2011. Persulfate activation by naturally occurring trace minerals. J. Hazard. Mater. 196, 153–159.
Tsitonaki, A., Smets, B.F., Bjerg, P.L., 2008. Effects of heat-activated persulfate oxidation on soil microorganisms. Water Res. 42, 1013–1022.
Waldemer, R.H., Tratnyek, P.G., Johnson, R.L., Nurmi, J.T., 2007. Oxidation of chlorinated ethenes by heat-activated persulfate: kinetics and products. Environ. Sci. Technol. 41, 1010–1015.
Wang, X., Qin, Y., Zhu, L., Tang, H., 2015. Nitrogen-doped reduced graphene oxide as a bifunctional material for removing bisphenols: synergistic effect between adsorption and catalysis. Environ. Sci. Technol. 49, 6855–6864.
Wang, Y., Sun, H., Ang, H.M., Tade, M.O., Wang, S., 2014. Facile synthesis of hierarchically structured magnetic MnO_2/$ZnFe_2O_4$ hybrid materials and their performance in heterogeneous activation of peroxymonosulfate. ACS Appl. Mater. Interf. 6, 19914–19923.
Wu, Y., Bianco, A., Brigante, M., Dong, W., Sainte-Claire, P., Hanna, K., Mailhot, G., 2015. Sulfate radical photogeneration using Fe-EDDS: influence of critical parameters and naturally occurring scavengers. Environ. Sci. Technol. 49, 14343–14349.
Xia, D., Ng, T.W., An, T., Li, G., Li, Y., Yip, H.Y., Zhao, H., Lu, A., Wong, P.K., 2013. A recyclable mineral catalyst for visible-light-driven photocatalytic inactivation of bacteria: natural magnetic sphalerite. Environ. Sci. Technol. 47, 11166–11173.
Xia, D., Li, Y., Huang, G., Fong, C.C., An, T., Li, G., Yip, H.Y., Zhao, H., Lu, A., Wong, P.K., 2015a. Visible-light-driven inactivation of Escherichia coli K-12 over thermal treated natural pyrrhotite. Appl. Catal. B Environ. 176–177, 749–756.
Xia, D., Shen, Z., Huang, G., Wang, W., Yu, J., Wong, P.K., 2015b. Red phosphorus: an earth-abundant elemental photocatalyst for "green" bacterial inactivation under visible light. Environ. Sci. Technol. 49, 6264–6273.
Xia, D., An, T., Li, G., Li, Y., Yip, H.Y., Zhao, H., Wong, P.K., 2016. Synergistic photocatalytic inactivation mechanisms of bacteria by graphene sheets grafted plasmonic Ag-AgX (X = Cl, Br, I) composite photocatalyst under visible light irradiation. Water Res. 99, 149–161.
Xia, D., Lo, I.M.C., 2016. Synthesis of magnetically separable Bi_2O_4/Fe_3O_4 hybrid nanocomposites with enhanced photocatalytic removal of ibuprofen under visible light irradiation. Water Res. 100, 393–404.
Xiong, X., Sun, B., Zhang, J., Gao, N., Shen, J., Li, J., Guan, X., 2014. Activating persulfate by Fe^0 coupling with weak magnetic field: performance and mechanism. Water Res. 62, 53–62.
Yan, J., Lei, M., Zhu, L., Anjum, M.N., Zou, J., Tang, H., 2011. Degradation of sulfamonomethoxine with Fe_3O_4 magnetic nanoparticles as heterogeneous activator of persulfate. J. Hazard. Mater 186, 1398–1404.
Yan, N., Liu, F., Xue, Q., Brusseau, M.L., Liu, Y., Wang, J., 2015. Degradation of trichloroethene by siderite-catalyzed hydrogen peroxide and persulfate: investigation of reaction mechanisms and degradation products. Chem. Eng. J. 274, 61–68.
Yang, Z., Kang, M., Ma, B., Xie, J., Chen, F., Charlet, L., Liu, C., 2014. Inhibition of U(VI) reduction by synthetic and natural pyrite. Environ. Sci. Technol. 48, 10716–10724.
Yuan, S., Liao, P., Alshawabkeh, A.N., 2014. Electrolytic manipulation of persulfate reactivity by iron electrodes for trichloroethylene degradation in groundwater. Environ. Sci. Technol. 48, 656–663.
Zeng, T., Zhang, X., Wang, S., Niu, H., Cai, Y., 2015. Spatial confinement of a Co_3O_4 catalyst in hollow metal-organic frameworks as a nanoreactor for improved degradation of organic pollutants. Environ. Sci. Technol. 49, 2350–2357.
Zhao, L., Sun, Z., Ma, J., Liu, H., 2010. Influencing mechanism of bicarbonate on the catalytic ozonation of nitrobenzene in aqueous solution by ceramic honeycomb supported manganese. J. Mol. Catal. A Chem. 322 (1–2), 26–32.
Zhang, S.H., Ye, C.S., Lin, H.R., Lv, L., Yu, X., 2015. UV disinfection induces a VBNC state in *Escherichia coli* and *Pseudomonas aeruginosa*. Environ. Sci. Technol. 49 (3), 1721–1728.
Zhang, T., Chen, Y., Wang, Y., Roux, J.L., Yang, Y., Croué, J.-P., 2014. Efficient peroxydisulfate activation process not relying on sulfate radical generation for water pollutant degradation. Environ. Sci. Technol. 48, 5868–5875.
Zhang, T., Zhu, H., Crou, J.-P., 2013. Production of sulfate radical from peroxymonsulfate induced by a magnetically separable $CuFe_2O_4$ spinel in water: efficiency, stability, and mechanism. Environ. Sci. Technol. 47, 2784–2791.
Zhang, Y., Tran, H.P., Du, X., Hussain, I., Huang, S., Zhou, S., Wen, W., 2017. Efficient pyrite activating persulfate process for degradation of *p*-chloroaniline in aqueous systems: a mechanistic study. Chem. Eng. J. 308, 1112–1119.
Zhong, H., Brusseau, M.L., Wang, Y., Yan, N., Quig, L., Johnson, G.R., 2015. *In-situ* activation of persulfate by iron filings and degradation of 1,4-dioxane. Water Res. 83, 104–111.